Radiation fog properties in two consecutive events under polluted and clean conditions in the Yangtze River Delta, China: A simulation study

Naifu Shao[1], Chunsong Lu[1], Xingcan Jia[2], Yuan Wang[3], Yubin Li[1], Yan Yin[1], Bin Zhu[1], Tianliang Zhao[1], Duanyang Liu[4,5], Shengjie Niu[1,6], Shuxian Fan[1], Shuqi Yan[4,5], Jingjing Lv[1]

[1]Key Laboratory for Aerosol-Cloud-Precipitation of China Meteorological Administration/Collaborative Innovation Centre on Forecast and Evaluation of Meteorological Disasters (CIC-FEMD), Nanjing University of Information Science & Technology, Nanjing, China
[2]Institute of Urban Meteorology, China Meteorological Administration (CMA), Beijing 100089, China
[3]Collaborative Innovation Centre for Western Ecological Safety, Lanzhou University, Lanzhou 730000, China.
[4]Nanjing Joint Institute for Atmospheric Sciences, Nanjing 211112, China
[5]Key Laboratory of Transportation Meteorology, CMA, Nanjing 210009, China
[6]College of Safety Science and Engineering, Nanjing Technology University, Nanjing 210009, China

Correspondence to: Chunsong Lu (luchunsong110@gmail.com)

Abstract. Aerosol–cloud interaction (ACI) in fog and planetary boundary layer (PBL) conditions play critical roles in the fog life cycle. However, it is not clear how ACI in the first fog (Fog1) affects the PBL, and subsequently affects ACI in the second fog (Fog2), which is important to understand the interaction between ACI and the PBL as well as their effects on fog properties. To fill this knowledge gap, we simulate two successive radiation fog events in the Yangtze River Delta, China, using the Weather Research and Forecasting model coupled with Chemistry (WRF-Chem). Our simulations indicate that the PBL conditions conducive to Fog2 formation are affected by ACI with high aerosol loading in Fog1; subsequently, the PBL promotes ACI in Fog2, resulting in a higher liquid water content, higher droplet number concentration, smaller droplet size, larger fog optical depth, wider fog distribution, and longer fog lifetime in Fog2 than in Fog1. This phenomenon is related to the following physical factors. The first factor involves meteorological conditions conducive to Fog2 formation, including low temperature, high humidity, and high stability. The second factor is the feedbacks between

28 microphysics and radiative cooling. A higher fog droplet number concentration increases the
29 liquid water path and fog optical depth, thereby enhancing long-wave radiative cooling and
30 condensation near the fog top. The third factor is the feedbacks between macrophysics,
31 radiation, and turbulence. A higher fog top presents stronger long-wave radiative cooling near
32 the fog top than near the fog base, which weakens temperature inversion and strengthens
33 turbulence, ultimately increasing the fog-top height and fog area.

34   In summary, under polluted conditions, ACI postpones the dissipation of Fog1 owing to
35 these two feedbacks and generates PBL meteorological conditions that are more conducive to
36 the formation of Fog2 than those prior to Fog1. These conditions promote the earlier formation
37 of Fog2, further enhancing the two feedbacks and strengthening the ACI in Fog2. Our findings
38 are critical for studying the interaction between aerosols, fog, and the PBL; moreover, they
39 shed new light on ACI.

1   Introduction

41 Fog comprises water droplets or ice crystals suspended above the ground (WMO, 1992). This
42 results in low visibility, which affects the human health, transportation, and power systems (Niu
43 et al., 2010). Uncertainties exist in fog forecasting (Zhou and Du, 2010; Zhou et al., 2011). An
44 important reason is that the physical processes of fog remain unclear because many processes
45 (aerosol activation, condensation, radiation, and turbulence) occur simultaneously and interact
46 with each other nonlinearly (Haeffelin et al., 2010), which affects fog properties (Mazoyer et
47 al., 2022) and impedes related parameterisation (Poku et al., 2021). To better understand the
48 physical processes of fog, Comprehensive studies based on observations and simulations have
49 been conducted to better understand the physical processes of fog (Fernando et al., 2021;
50 Gultepe et al., 2014; Guo et al., 2015; Hammer et al., 2014; Liu et al., 2011; Price et al., 2018;
51 Shen et al., 2018; Wang et al., 2021). The critical roles of aerosols and planetary boundary layer

52 (PBL) in these processes have been shown (Boutle et al., 2018; Niu et al., 2011; Quan et al.,
53 2021).

54 Since fog is a special type of cloud (Guo et al., 2021; Kim and Yum, 2010, 2013; Wang et
55 al., 2023), aerosol–fog interaction is expected to share similarities with aerosol–cloud
56 interaction (ACI). The ACI in fog reflects the response of fog properties to changes in aerosol
57 loading. Studies on ACI revealed that increasing aerosol loading increased cloud droplet
58 concentration, thereby increasing the cloud optical depth under a constant liquid water content
59 (LWC) (Garrett and Zhao, 2006; Twomey, 1977; Wang et al., 2013; Wang et al., 2018; Zhao
60 and Garrett, 2015). Various continental fog observation projects showed that fog microphysical
61 properties were significantly affected by aerosol loading (Mazoyer et al., 2019; Niu et al., 2011;
62 Quan et al., 2011; Wang et al., 2021). For instance, in polluted fog observations, Quan et al.
63 (2011) found that the fog droplet number concentration (N_d) was higher than 1,000 cm^{-3} and
64 effective radius (R_e) was approximately 7 μm in the North China Plain. In clean fog
65 observations, Wang et al. (2021) showed that N_d was smaller than 100 cm^{-3} and R_e was
66 approximately 9 μm in the tropical rainforest in Xishuangbanna, China. Several simulation
67 studies reproduced these observations, and demonstrated the complex impact of ACI on fog
68 micro- and macrophysics (Jia et al., 2019; Maalick et al., 2016; Stolaki et al., 2015; Yan et al.,
69 2020). Regarding fog microphysics, increasing aerosol loading in the simulations increased N_d
70 and LWC due to increased activation and condensation (Jia et al., 2019; Stolaki et al., 2015;
71 Yan et al., 2020). Regarding fog macrophysics, several modelling studies reported that
72 increasing aerosol loading increased the fog-top height (Jia et al., 2019; Stolaki et al., 2015)
73 and prolonged the fog lifetime by delaying its dissipation (Quan et al., 2021; Yan et al., 2021).

74 Furthermore, previous studies found that meteorological conditions played crucial roles in
75 aerosol–cloud interaction as well as cloud macro- and microphysics (Ackerman et al., 2004;
76 Kumar et al., 2017; Kumar et al., 2021; Liu et al., 2019; Liu et al., 2020; Toll et al., 2019).

Similarly, studies on fog showed that ACI was affected by meteorological conditions in the PBL (e.g., radiation, thermodynamics, and dynamics), which further affected fog micro- and macrophysics (Haeffelin et al., 2010). Previous studies showed that radiative cooling was an important factor in temperature inversion that provided stable conditions for fog formation (Fitzjarrald and Lala, 1989; Holets and Swanson, 1981; Roach et al., 1976). According to Zhou and Ferrier (2008), turbulence may suppress or deepen the fog-top height, which was related to the critical turbulence coefficient. The critical turbulence coefficient was the turbulence threshold for diagnosing whether turbulence suppressed fog or not. When the turbulence intensity within the fog did not exceed the critical turbulence coefficient, the fog persisted; however, when it surpassed its threshold, the fog dissipated (Zhou and Ferrier, 2008). When temperature inversion was weak, excessive vertical turbulent mixing delayed fog formation (Maronga and Bosveld, 2017). However, when temperature inversion was sufficiently strong, vertical turbulent mixing at the middle and fog base increased the fog-top height, as suggested by observations (Ye et al., 2015) and simulations (Porson et al., 2011). Consequently, turbulence may impact fog macrophysics. Moreover, aerosols were reported to affect turbulence, thereby impacting fog macrophysics (Jia et al., 2019; Quan et al., 2021). A qualitative analysis, conducted in a previous study, revealed that aerosols promoted turbulence and horizontal distribution because of weaker temperature inversion (Jia et al., 2019).

Previous studies typically focused on either a single fog event or analysed multiple fog events statistically; however, several studies noted that LWC, N_d, and liquid water path (LWP) in a latter fog event exhibited larger values compared to those for the preceding fog event (Quan et al., 2011; Wærsted et al., 2017). What are the physical mechanisms behind the property changes during two successive fog events? Furthermore, which fog event has macro- and microphysical properties that are more sensitive to aerosol loading, i.e., experiencing a stronger ACI? What are the mechanisms underlying the interactions between ACI and the PBL? To

answer these questions, two successive radiation fog events in the Yangtze River Delta (YRD) region of China are simulated in this article using the Weather Research and Forecasting model coupled with Chemistry (WRF-Chem). The two fog events provide an excellent opportunity to investigate ACI under polluted conditions as a chain. This involves analysing how high aerosol loading affects properties in the first fog event, how the properties in the first polluted fog event affect radiation and PBL structure, and finally, how radiation and the PBL affect properties and ACI in the second fog event under polluted conditions. Additionally, since fog is a special type of cloud near the ground, studying the evolution of ACI in fog aids in examining the progression of ACI in cloud, which is critical for climate prediction (Boutle et al., 2018; Vautard et al., 2009) .

The rest of the article is organized as follows. Section 2 presents descriptions of the two successive fog events, experimental design, and data source. Section 3 presents simulation evaluation. Section 4 shows larger aerosol-induced changes in Fog2 than in Fog1. Section 5 presents the physical mechanisms underlying the larger aerosol-induced changes in Fog2 than in Fog1. Finally, Section 6 summarises the conclusions of this study.

2 Experimental design and data source

Here, we study how radiation fog properties are affected by high aerosol loading and PBL meteorological conditions in two successive events in the YRD region. Before fog events in the YRD, the $PM_{2.5}$ mass concentration was over 100 μg m^{-3} due to anthropogenic emissions (Zhu et al., 2019). On 26 and 27 November 2018, two successive radiation fog events occurred in northern YRD. The first fog event is called Fog1, and the second is called Fog2. Ground-based observations at the Nanjing site (32.2 °N 118.7 °E) show that two fog events (visibility < 1,000 m) are accompanied by high relative humidity, low temperature, and weak wind speed (Fig. 1). As shown in Fig. S1, the surface is controlled by a high–pressure system with cold and moist

air in northern YRD at 20:00 local standard time (LST) (LST = Universal Time Coordinated + 8 h) on 26 and 27 November 2018. WRF-Chem (version 4.1.3) is used to simulate the two successive radiation fog events. WRF-Chem couples physical and chemical processes; therefore, it has been widely used to study ACI (Jia et al., 2019; Lee et al., 2016; Yan et al., 2020; Yan et al., 2021). The model is integrated from 14:00 LST on 24 November 2018 to 14:00 LST on 27 November 2018, with the first 24 hours regarded as the spin-up time. As shown in Fig. S2, the model is configured using three nested domains, and all domain centres are located in Nanjing. The three nested domains are 90×122, 118×142, and 130×154 grid cells with resolutions of 27, 9, and 3 km, respectively. The simulation area covers the major weather system affecting the YRD. The model includes 36 vertical levels, of which 17 layers are located at the lowest 500 m above the ground level. Moreover, Yang et al. (2019) noted a better fog simulation performance when the bottom layer was 8 m above the ground since this layer affected the fog and surface flux interaction. Consequently, in this study, we set the bottom layer of the model to 8 m. The model is driven by the National Centre for Environmental Prediction (NCEP) Final (FNL) $1° \times 1°$ reanalysis data (https://rda.ucar.edu/datasets/ds083.2/) (Ding et al., 2019; Jia et al., 2019). The Multiresolution Emission Inventory for China (MEIC) database (http://meicmodel.org) is used for anthropogenic emissions in the model (Li et al., 2017a; Zheng et al., 2018).

Table 1 lists the parameterisation schemes of physical processes used in this study. The microphysics scheme is Morrison (Morrison et al., 2005) coupled with the activation scheme (Abdul-Razzak, 2002). The PBL scheme is MYNN2.5 (Nakanishi and Niino, 2009). Turbulence is parameterised in the MYNN2.5 scheme and there is also a sub-grid cloud parameterisation (Chaboureau and Bechtold, 2002) in the MYNN2.5 scheme. The radiation schemes are coupled with the aerosol–cloud–radiation interactions. The long- and short-wave radiation schemes are RRTMG (Iacono et al., 2008) and Goddard (Matsui et al., 2020),

respectively. The cumulus scheme is Grell 3D (Grell and Dévényi, 2002). The chemistry schemes are MOSAIC-4 bins (Zaveri et al., 2008) and CBMZ (Zaveri and Peters, 1999).

For model evaluation, meteorological data are retrieved from the China Meteorological Administration (http://www.nmic.cn/). The cloud product (level 2 full-disk cloud property data) from the Himawari-8 geostationary satellite is used (Bessho et al., 2016; Iwabuchi et al., 2018) (https://www. eorc.jaxa.jp/ptree/index.html). The quality of the Himawari cloud product is reliable because this product has been evaluated against the Moderate Resolution Imaging Spectroradiometer (MODIS) (Bessho et al., 2016; Letu et al., 2020) and cloud profiles from aircraft measurements (Zhao et al., 2020). Spatial resolution of the Himawari cloud product is $0.05° \times 0.05°$ (Yang et al., 2020). $PM_{2.5}$ mass concentration data are obtained from the Ministry of Environmental Protection (https://quotsoft.net/air/).

To investigate the aerosol-induced changes in fog macro- and microphysics, one control run and two sensitivity tests are conducted: EXP1, EXP2, and EXP3, respectively. High and low emissions indicate polluted and clean conditions, respectively. The differences indicate the aerosol effect on fog properties. In EXP1, the emission intensity is obtained directly from the MEIC database to simulate fog under polluted conditions. In EXP2, the emission intensity is multiplied by 0.05 to simulate fog under clean conditions, as described by Jia et al. (2019) and Yan et al. (2021). In EXP3, Fog1 occurs under clean conditions (5% of emission from the MEIC database) and Fog2 occurs under polluted conditions (the default emission from the MEIC database). According to Fog1 dissipation time, clean conditions change to polluted conditions at 12:00 LST on 26 November 2018. Compared with the difference between EXP1 and EXP2, the difference between EXP3 and EXP2 reveals whether the fog properties and ACI with higher aerosol loading in Fog1 affects those in Fog2.

3   Simulation evaluation

Simulation evaluations for temperature, relative humidity, and wind speed are shown in Fig. 2. The correlation coefficients of 2 m temperature (T_{2m}), 2 m relative humidity (RH_{2m}), and 10 m wind speed (WS_{10m}) between the simulations and observations are 0.9, 0.9, and 0.6, respectively, passing the significance test at 99%. Therefore, the simulations are generally consistent with the observations. The mean bias (MB) of T_{2m}, RH_{2m}, and WS_{10m} between the simulations and observations are 1.0 °C, 2.7%, and 0.4 m s^{-1}, respectively, consistent with evaluation results in studies by Hu et al. (2021), Gao et al. (2016), and Yang et al. (2022). Figure 3 shows the evaluation of $PM_{2.5}$ distribution, and Table 2 summarises statistics of the mean mass concentration of $PM_{2.5}$ based on the method proposed by Boylan and Russell (2006). The normalised mean bias (NMB), normalised mean error (NME), mean fractional bias (MFB), and mean fractional error (MFE) between the simulations and observations are 25%, 30%, 24%, and 28%, respectively (Eqs. S3–S6 in the supplement). Although the $PM_{2.5}$ mass concentration is overestimated, it remains within a reasonable range (Shu et al., 2021; Yang et al., 2022; Zhai et al., 2018).

Figure 4 shows the evaluation of fog spatial distribution. The simulated fog optical depth distribution is compared with the Himawari-8 cloud optical depth products at 08:00 LST on 26 and 27 November 2018, respectively. To identify observed fog at ground-based stations (the black circles in Fig. 4), we apply two criteria: visibility less than 1 km and relative humidity greater than 90% (Yan et al., 2020). Qualitatively, the value of fog optical depth and the fog spatial distribution in the simulation are roughly similar to those observed by the Himawari satellite and at ground-based stations. Likewise, Lee et al. (2016) evaluated fog distribution simulations against satellite-derived cloud optical depth from satellite and concluded that the distributions of simulations and observations were generally comparable to each other.

198   Further, to quantitatively evaluate the simulation, the Heidke skill score (HSS) is
199   calculated as follows (Barnston, 1992):

200
$$HSS = \frac{2(ad - bc)}{(a+c)(c+d)+(a+b)(b+d)} \tag{1}$$

201   Elements a–d are determined by the occurrence of fog at observation stations located in domain
202   03 and the closest model grids to those observations, as shown in Table 3. If fog events are both
203   observed at stations and simulated at the closest model grids, we recognize those as "hits" and
204   a in Eq.1 represents the total number of "hits" during the entire fog event. Similarly, d represents
205   the number of "correct negatives" for the correct non-event simulations. On the other hand, if
206   fog events are simulated but not observed, we recognize those as "false alarms" and b represents
207   the total number of "false alarms" during the entire fog event. Conversely, c represents the total
208   number of "misses", which indicates that fog events are observed but not simulated. The criteria
209   of observed fog are shown in the last paragraph. Simulated foggy grids are classified based on
210   three criteria (Jia et al., 2019; Zhao et al., 2013): fog water mixing ratio over 0.01 g kg^{-1}, N_d
211   greater than 1 cm^{-3}, and fog base touching the ground. The perfect HSS score is 1.0, indicating
212   that simulations are identical to observations. Here, the HSS score are 0.34 and 0.36 in Fog1
213   and Fog2, respectively, which are close to previous reports (Mecikalski et al., 2008; Xu et al.,
214   2020; Yamane et al., 2010). Therefore, the model generally captures the fog spatial distribution.

215   **4   Larger aerosol-induced changes in Fog2 than in Fog1**

216   Here, we analyse the fog macro- and microphysical characteristics under clean and polluted
217   conditions (Fig. 5). To ensure sufficient sample size for statistical analysis, only data with the
218   fog area fraction larger than 5% are analysed. The fog area fraction is calculated as the number
219   of foggy grid cells divided by the total number of grids in domain 03. We also test other

220 thresholds, 1%, 2.5%, 7.5%, and 10% (Fig. S3). The results are similar to those based on the
221 threshold of 5%.

222  The ratios of changes between the polluted and clean conditions reveal that high aerosol
223 loading affects fog macro- and microphysical properties in Fog1 and Fog2 (Fig. 5a). Compared
224 to fog microphysics under clean conditions, N_d and LWC in Fog1 increase by respectively 463.0%
225 and 81.7%; however, R_e decreased by 32.1% under polluted conditions. Furthermore, because
226 of the ACI, N_d and LWC in Fog2 increase by respectively 672.4% and 113.5%; however R_e
227 decreases by 40.0%. Therefore, aerosol-induced changes in Fog2 are larger than those in Fog1,
228 as shown in Fig. 5a (N_d: 209.5%, LWC: 31.8%, and R_e: −6.9%). Similarly, aerosol-induced
229 changes in fog macrophysics are larger in Fog2. Compared with values under clean conditions,
230 the fog area, fog-top height, and duration in Fog1 increase by respectively 23.1%, 109.6%, and
231 20.0% under polluted conditions; the corresponding values in Fog2 are larger (34.9%, 350.5%,
232 and 25.0%, respectively). In addition, LWP and fog optical depth (τ_c) exhibit similar trends.
233 With a similar trend between observation and simulation, Figure S4 shows that aerosol mass
234 concentration is similar before Fog1 and Fog2 formation, and aerosol number concentration
235 before Fog2 is less than that before Fog1 formation. Therefore, changes in aerosol concentration
236 are not the main reason for the increase in aerosol-induced changes in the two fog properties.
237 To determine whether ACI under polluted conditions leads to an increase in aerosol-induced
238 changes in Fog1 and Fog2, we design a sensitivity test called EXP3, as mentioned above.
239 Furthermore, to quantitatively evaluate the strength of ACI in the two fog events, we examine
240 the responses of τ_c to changes in N_d (Eq. 2) (Ghan et al., 2016):

241 $$\frac{\Delta \ln \tau_c}{\Delta \ln N_d} = \frac{\Delta \ln LWP}{\Delta \ln N_d} - \frac{\Delta \ln R_e}{\Delta \ln N_d} \qquad (2)$$

242  Based on the similar aerosol concentration background (Fig. S4), the responses of τ_c to
243 changes in N_d quantitatively confirm which fog has stronger ACI. As shown in Table 4, the

strength of ACI in Fog2 (1.32) is larger than that in Fog1 (0.98). If Fog1 occurs under clean conditions and Fog2 occurs under polluted conditions (EXP3), ACI in Fog2 is 1.17, which is lower than that in EXP1 (1.32). This implies that high aerosol loading in Fog1 enhances ACI in Fog2. Relative changes in the above properties between Fog1 and Fog2 are calculated as (Fog2 − Fog1)/Fog1. The values of $\Delta \ln \tau_c / \Delta \ln N_d$, $\Delta \ln LWP / \Delta \ln N_d$, as well as $-\Delta \ln R_e / \Delta \ln N_d$ are 34.7%, 42.1%, and 9.1% larger in Fog2 than in Fog1, respectively. These numbers quantitatively confirm stronger ACI in Fog2 and indicate that LWP is the dominant factor for enhancing ACI. LWP depends on the fog-top height and LWC. As shown in Fig. 5a, when aerosol loading changes from clean to pollution, the rate of increase in fog-top height in Fog2 (350.5%) is much larger than that in Fog1 (109.6%). Although the increase in LWC in Fog2 (113.5%) is also larger than that in Fog1 (81.7%), the magnitude of increase in LWC is smaller than that increase in fog-top height, indicating that ACI are more sensitive to fog-top height than to LWC.

Fog duration is determined by the time of fog formation and dissipation, which is primarily extended because high aerosol loading delays fog dissipation, as reported previously (Jia et al., 2019; Quan et al., 2021). In this study, high aerosol loading not only delays fog dissipation but also promotes earlier fog formation, particularly during Fog2 (Fig. 5b). Fog formation is related to the PBL conditions which are affected by ACI. To investigate the aerosol effect on the Fog2 formation stage, fog spatial distribution at the formation stage from 19:00 LST to 21:00 LST on 26 November is examined, as shown in Figure 6. The fog area is rather small at 19:00 LST under both polluted and clean conditions. At 20:00 LST, fog formation is similar under both polluted and clean conditions in grid cells located outside the black box. However, inside the black box, there are several foggy grid cells under polluted conditions. At 21:00 LST, fog area in the black box further expands under polluted conditions. However, there is almost no fog in the black box at 20:00 and 21:00 LST under clean conditions. Therefore, high aerosol loading

269 promotes earlier formation of Fog2, which is primarily caused by meteorological conditions in
270 the PBL inside the black box. In addition, the fog area outside the black box is larger under
271 polluted conditions than under clean conditions, which is mainly related to the stronger
272 turbulence diffusion under polluted conditions. A detailed analysis is presented in Sect. 5.

273 ## 5   Physical mechanisms underlying the larger aerosol-induced changes in Fog2 than in
274 Fog1

275 ### 5.1.   More conducive meteorological conditions to Fog2 formation

276 Meteorological conditions in the PBL affect fog formation time and ACI during fog events. As
277 shown in Table 5, under clean conditions, RH_{2m} before Fog2 formation is higher and PBL
278 height (PBLH) is lower than those before Fog1 formation in domain 03. Polluted conditions
279 yield similar results. Furthermore, compared with the difference in aerosol-induced changes in
280 RH_{2m} and PBLH before fog formation, RH_{2m} increases by 6% and PBLH decreases by 92 m
281 under polluted conditions, which is larger than those (RH_{2m}: 4% and PBLH: −59 m) under clean
282 conditions. Therefore, high aerosol loading generates meteorological conditions more
283 conducive to Fog2 formation during the two successive fog events.

284 To further analyse how high aerosol loading promotes Fog2 formation, we focus on the
285 black box in Fig. 6, as described in Sect. 4 and by Yan et al. (2021). The regional average
286 differences in the total optical depth (τ_t), downwelling short-wave radiation (SW) at the ground,
287 T_{2m}, PBLH, RH_{2m}, and water vapour mixing ratio (Qv_{bot}) at the model bottom layer (8 m) in
288 the black box between polluted and clean conditions are calculated (Fig. 7). Compared with
289 clean conditions, the larger τ_t (mainly due to larger τ_c) and delayed fog dissipation in polluted
290 conditions reduce short-wave radiation reaching the ground (from −46 W m^{-2} to −121 W m^{-2})
291 during the Fog1 dissipation time. This leads to a decrease in T_{2m} (from −0.2 °C to −1 °C) and

PBLH (from −42 m to −118 m), which further prolongs fog duration (Fig. 7). Notably, Qv_{bot} under polluted conditions is lower than that under clean conditions before the complete dissipation of Fog1, because of reduced fog water evaporation. When the fog dissipates completely, the lower PBLH accumulates more water vapour, increasing Qv_{bot} and RH_{2m}. The positive feedbacks between ACI and PBL are similar to the feedbacks between high aerosol loading and the PBL reviewed by Li et al. (2017b). Furthermore, the feedback mechanism between high aerosol loading and PBL introduced by Zhong et al. (2018) supports the daytime feedbacks between fog and the PBL in the present study. Additionally, aerosol extinction is also considered in τ_t. Whether aerosol optical depth (AOD) affects PBL significantly should also be discussed. As shown in Table 5, RH_{2m} and PBLH before Fog1 on 25 November under clean conditions are 76% and 669 m, respectively, similar to those under polluted conditions (76% and 670 m, respectively). Therefore, it is unlikely that aerosol-meteorology interaction leads to the meteorological differences in Fig. 7. In addition, a previous study (Yan et al., 2021) also noted that aerosol–fog interaction was more remarkable than aerosol–radiation interaction. Therefore, lower temperature, higher relative humidity, and higher stability result from ACI in Fog1 under polluted conditions, contributing to the earlier formation of Fog2.

Larger τ_c and delayed dissipation result in lower temperature, higher relative humidity, and higher stability by affecting solar radiation during the daytime. How are these conducive conditions maintained after the sunset around 17:00 LST? Figure 8a shows that cold advection is the major reason for the difference in temperature between polluted and clean conditions. We further seek to unveil the reason cold advection is stronger under polluted conditions. Figure 8b shows a cold centre, with wind diverging outwards. The cold centre is related to lower temperature under polluted conditions due to larger τ_c and longer duration in Fog1. Likewise, Steeneveld and De Bode (2018) noted that fog appeared earlier with cold advection. In addition,

316 lower PBLH induced by high aerosol loading promote the maintenance of higher humidity and
317 stability.

318   Overall, due to ACI at the Fog1 dissipation stage, the meteorological conditions are more
319 conducive for promoting Fog2 formation. Furthermore, this interaction enhances the feedbacks
320 in the fog physical processes, thus leading to a stronger ACI in Fog2. Details are discussed in
321 Sect. 5.2 and 5.3.

322

5.2. Feedbacks between microphysics and long-wave cooling

324 Section 5.1 reveals the mechanism through which ACI in Fog1 leads to meteorological
325 conditions more conducive to Fog2 formation. In Sect. 5.2, we demonstrate how conducive
326 meteorological conditions play a fundamental role in promoting feedbacks between
327 microphysics and long-wave cooling, resulting in a stronger ACI in Fog2.

328   As shown in Fig. 5a, aerosol-induced changes in N_d and LWC during Fog2 are larger than
329 those during Fog1 because lower temperature and higher humidity are more conducive for
330 aerosol activation and fog condensation (Petters and Kreidenweis, 2007; Simmel and Wurzler,
331 2006). Owing to competition for available water vapour (Mazoyer et al., 2022; Yum and
332 Hudson, 2005), R_e in Fog2 is smaller than that in Fog1. As shown in Fig. 9a, LWP is larger
333 under polluted conditions than that under clean conditions, particularly for Fog2. The average
334 LWP in Fog1 and Fog2 under polluted conditions are 11.6 g m^{-2} and 24.3 g m^{-2}, respectively.
335 When LWP is less than 20 g m^{-2}, vertically integrated long-wave cooling and short-wave
336 heating are stronger under polluted conditions than those under clean conditions (Fig. 9b). This
337 is similar to the results from Petters et al. (2012) and Prabhakaran et al. (2023). Because N_d
338 shows a similar trend with LWP (Fig. S5), the dependence of heating and cooling rates on
339 droplet concentration is consistent with the results based on LWP. Additionally, increased τ_c

340 in Fog2 triggers stronger positive feedbacks between microphysics and long-wave cooling,
341 further enhancing cooling, activation, and condensation and thereby increasing N_d and LWC.
342 Jia et al. (2019) emphasised that high aerosol loading promoted these positive feedbacks. This
343 study further highlights the synergistic effects of high aerosol loading and meteorological
344 conditions on the enhancement of positive feedbacks, which promotes ACI in Fog2.

345   To better understand how the above positive feedbacks affect ACI, Fig. 10 presents the
346 average extinction coefficient through the fog, that is, τ_c at per unit height ($\tau_c/\Delta h$), radiative
347 cooling rate (T_{LW}), condensational growth rate (LWC_{COND}), and LWC tendency due to vertical
348 mixing (LWC_{mixing}) in the two successive fog events. Radiative cooling is the strongest near the
349 fog top and weakest near the fog base (Ducongé et al., 2020; Mazoyer et al., 2017; Wærsted et
350 al., 2017). Consequently, LWC_{COND} and LWC_{mixing} both follow similar profiles in response to
351 radiative cooling. Therefore, if the vertical profiles of the three terms use absolute height, they
352 will be distorted. To overcome this problem, physical quantities are normalised by the fog-top
353 height. Compared with those in Fog1, larger extinction coefficient (Fig. 10a-b), stronger long-
354 wave radiative cooling (Fig. 10c-d), and more condensation (Fig. 10e-f) near the fog top are
355 noted in Fog2 because of the conducive conditions to Fog2 formation, which further increases
356 LWC, fog-top height in Fog2 (black and purple lines) as well as LWP. Enhancement of these
357 parameters indicate that the feedbacks between microphysics and long-wave cooling are
358 stronger in Fog2 than in Fog1. As a result, ACI is stronger in Fog2 than in Fog1, due to
359 favourable PBL conditions caused by ACI in Fog 1. In addition, as shown in Fig. 10g-h, vertical
360 mixing transports fog water from the fog top to the fog base, and the strength of this
361 transportation is stronger in Fog2 than in Fog1, because of stronger turbulent kinetic energy
362 (TKE) in Fog2. The effect of TKE on fog is analysed in Sect. 5.3.

5.3. Feedbacks between macrophysics, radiation, and turbulence

Section 5.2 analyses the microphysics-related mechanisms underlying a stronger ACI in Fog2. This subsection not only focuses on macrophysics and its feedbacks with radiation and turbulence but also discusses how the combined effects of high aerosol loading and meteorological conditions impact the feedbacks and enhance ACI in Fog2, compared with those in Fog1. Briefly, fog macrophysics involves duration and distribution. The reason why the duration of Fog2 is longer than that of Fog1 is due to the earlier formation of Fog2, which is induced by meteorological conditions more conducive to Fog2 formation, as discussed in Sect. 5.1. The reason for the wider distribution (fog-top height and fog area) is discussed here.

5.3.1 Effects of macrophysics on radiation

Meteorological conditions more conducive to Fog2 formation and ACI promote condensation near the fog top (Fig. 10d, f), thereby raising the fog-top height in Fog2 compared with that in Fog1 (black and purple lines in Fig. 10). Therefore, both fog-top height and τ_c in Fog2 are higher than those in Fog1. Compared with that in Fog1, the higher τ_c in Fog2 enhances cooling near the fog top and downwelling long-wave radiation, weakening the cooling at the fog base than near the fog top (Fig. 10c). Additionally, the horizontal distribution of Fog2 is wider than that of Fog1 (Fig. 5b). Therefore, more foggy grid cells show more radiative cooling near the fog top and downwelling long-wave radiation at the fog base in Fog2.

5.3.2 Effects of radiation on turbulence

The above analysis reveals the mechanism underlying the effects of meteorology and ACI on radiation in fog. How does radiation affect stability and turbulence (i.e., TKE)? To answer this question, we must know the dominant factors contributing to TKE, as described in the following TKE budget equation:

$$\frac{\Delta TKE}{\Delta t} = TKE_{\text{shear}} + TKE_{\text{buoy}} - TKE_{\text{diss}} + TKE_{\text{mixing}} \tag{3}$$

where $\Delta TKE/\Delta t$ is the TKE tendency with time (Fig. 11b), and the four terms on the right side of Eq. (3) are contributors to TKE, including wind shear (Fig. 11c), buoyancy (Fig. 11d), dissipation (Fig. 11e), and vertical mixing (Fig. 11f). Detailed equations of these contributions to TKE are provided in supplementary information (Eqs. S5-S8) (Nakanishi and Niino (2009)).

As shown in Fig. 11a, TKE in Fog2 is stronger than that in Fog1, particularly under polluted conditions. Since the vertical mixing term is one order smaller than the others, it is negligible (Fig. 11f). At night, only the shear term is positive and, therefore, the main contributor to TKE (Fig. 11c), consistent with the speculations of Kim and Yum (2012). However, the dominant term driving the differences in TKE between polluted and clean conditions is buoyancy (Fig. 11d). As shown in Fig. 11b, $\Delta TKE/\Delta t$ is larger under polluted conditions than under clean conditions. Meanwhile, the shear term is smaller but the buoyancy term is larger under polluted conditions than under clean conditions, and the dissipation term is similar between the two conditions. Therefore, the buoyancy term is the main factor that increase TKE under polluted conditions, corroborating the qualitative speculations by Jia et al. (2019). This is particularly true for Fog2. In addition, at daytime, $\Delta TKE/\Delta t$ is weaker under polluted conditions, because higher τ_c reduces short-wave radiation reaching the surface. These results are consistent with the higher stability during the dissipation stage under polluted conditions, as described in Sect. 5.1.

After confirming the importance of the buoyancy term, we analyse the effect of radiation on buoyancy and then on TKE. Buoyancy contributions to TKE are determined by temperature inversion in the PBL at the night time. As shown in Fig. 12a-b, temperature inversion is close to the surface. With the effect of ACI, much stronger radiative cooling leads to a more rapid temperature drop at the fog top than at the fog base (Fig. 12c), thereby causing weaker

410 temperature inversion under polluted conditions. Therefore, stability is weaker and TKE is
411 larger under polluted conditions, particularly in Fog2.

5.3.3 Effects of turbulence on macrophysics

413 Previous observations (Liu et al., 2010; Román-Cascón et al., 2016) and large eddy simulations
414 (Bergot, 2013; Mazoyer et al., 2017; Nakanishi, 2000) showed that turbulence could increase
415 the fog-top height. In this study, we note that increasing TKE increases fog-top height (black
416 and purple lines in Fig. 10) and fog area (Fig. 5b), which is consistent with observations of Jia
417 et al. (2019) and Quan et al. (2021). The increased fog-top height increases TKE by promoting
418 radiative cooling near the fog top and weakening temperature inversion. This reflects the
419 feedbacks between macrophysics, radiation, and turbulence. Overall, owing to meteorological
420 conditions more conducive to Fog2 formation, the feedbacks are stronger in Fog2 than in Fog1.

6   Conclusion

422 To explore the interactions between the PBL and ACI, as well as their effects on fog properties,
423 WRF-Chem 4.1.3 is used to simulate two successive radiation fog events that occurs in the
424 northern YRD region in China on 26 and 27 November 2018. Two fog events simulation (Fog1
425 and Fog2) well reproduces the observed results.

426   The results show higher LWC, higher N_d, smaller R_e, higher fog-top height, longer duration,
427 wider spatial distribution, higher LWP, and higher τ_c under polluted conditions than under clean
428 conditions. Aerosol-induced changes in micro and macro-physical properties are more
429 significant in Fog2 than in Fog1. When Fog1 occurs under clean conditions, the response of
430 Fog2 to high aerosol loading becomes weaker. Therefore, ACI with high aerosol loading in
431 Fog1 promotes aerosol-induced changes in Fog2. A conceptual diagram is proposed to describe

the mechanism of fog property changes as well as ACI evolution during two successive radiation fog events (Fig. 13). Moreover, the mechanisms of changes in fog properties and ACI evolution are discussed based on the synergistic effects of aerosols and meteorological conditions. The microphysics–radiation feedbacks and macrophysics–radiation–turbulence feedbacks delay Fog1 dissipation, generating more conducive conditions for promoting the earlier formation of Fog2. Furthermore, the microphysics–radiation feedbacks and macrophysics–radiation–turbulence feedbacks are strengthened in Fog2 due to the conditions more conducive to Fog2 formation, enhancing ACI in Fog2 compared with those in Fog1. Detailed mechanisms are summarised below, including meteorological conditions and the two types of feedbacks.

First, meteorological conditions before Fog2 formation are more conducive than those before Fog1 formation, which play fundamental roles in changing fog properties and enhancing ACI during two fog events. This is related to the delayed dissipation of Fog1 induced by τ_c. During Fog1 dissipation (daytime), the cooling effect caused by the higher τ_c contributes to the lower temperature, higher relative humidity, and higher stability. At night, cold advection near the ground is enhanced. Meanwhile, the temperature remains low, forming a cold centre, due to low daytime temperature. Moreover, the surface wind diverges outward from the cold centre, strengthening the cold advection. Ultimately, the meteorological conditions induced by high aerosol loading are more conducive for promoting the earlier formation as well as a longer duration of Fog2 than of Fog1.

Second, the positive feedbacks between microphysics and radiative cooling are crucial physical mechanisms for changing fog properties and enhancing ACI. In Fog2, high aerosol loading and more conducive meteorological conditions synergistically promote fog microphysics. Lower temperature and higher relative humidity promote aerosol activation and condensation. Consequently, N_d, LWP, and τ_c are higher, whereas R_e is smaller, in Fog2 than in

Fog1. Radiative cooling and heating within the fog layer depend on LWP and N_d. When LWP in fog is less than 20 g m^{-2}, and higher aerosol loading enhances vertically integrated cooling and heating in optically thin fog. These variations in microphysics lead to stronger long-wave radiative cooling and condensational growth near the top of Fog2. Therefore, the positive feedbacks between microphysics and radiation are stronger in Fog2, which further promote stronger ACI.

Finally, the feedbacks between fog macrophysics, radiation, and turbulence affect fog properties. Under polluted conditions, the higher fog top strengthens the fog-top long-wave radiative cooling and then reduces the strength of temperature inversion near the surface and enhances turbulence. Stronger turbulence further increases the fog-top height and fog area. Because of meteorological conditions more conducive to Fog2 formation, the feedbacks are stronger in Fog2 than in Fog1, contributing to the enhancement of ACI.

This study focuses on a two-day radiation fog event in the Yangtze River Delta, China, which has a large population. The conclusions are expected to be applicable to radiation fog events in this region and other regions with similar human activities. It would be interesting to see if similar conclusions can be found in other fog types (e.g., advection fog) in other regions (e.g., ocean). Furthermore, there are large uncertainties in the aerosol–cloud interaction (Fan et al.,2016; Guo et al., 2018; Rosenfeld et al., 2019; Seinfeld et al., 2016; Zhu and Penner, 2020; Zhu et al., 2019). The findings of our study offer novel insights into the potential involvement of mechanisms responsible for evolution of ACI, particularly for stratus, which is similar to fog.

Data and code availability. The data repositories have been listed in Sect. 2. Codes are accessed by contacting Chunsong Lu via luchunsong110@gmail.com.

Author contributions. NS performed the data analysis, model simulation, and article writing. CL proposed the idea, supervised the work, and revised the article. XJ and YW both took part

in revising the article and gave suggestions. Ground-based observation data were provided by XJ and DL. YL supervised the analysis of the turbulence kinetic energy budget. TZ supported the work that anthropogenic emissions were driven by Multiresolution Emission Inventory for China (MECI). SN provided financial support. NS prepared the article with help from YY, BZ, SF, SY, and JL.

Competing interests. The authors in this article declare that they have no conflict of interest with others.

Acknowledgements. This Article is supported by the National Key Scientific and Technological Infrastructure project "Earth System Science Numerical Simulator Facility" (EarthLab), and we acknowledge the High Performance Computing Centre of Nanjing University of Information Science & Technology for their support of this work.

Financial support. This research has been supported by the National Natural Science Foundation of China (grant nos. 42027804, 41775134, 41975181, 42205072) and the Science and Technology Planning Project of Gansu Province (grant no. 22JR5RA445).

References

Abdul-Razzak, H.: A parameterization of aerosol activation 3. Sectional representation, J. Geophys. Res., 107, https://doi.org/10.1029/2001jd000483, 2002.

Ackerman, A. S., Kirkpatrick, M. P., Stevens, D. E., and Toon, O. B.: The impact of humidity above stratiform clouds on indirect aerosol climate forcing, Nature, 432, 1014-1017, https://doi.org/10.1038/nature03174, 2004.

Barnston, A. G.: Correspondence among the Correlation, RMSE, and Heidke Forecast Verification Measures; Refinement of the Heidke Score, Weather Forecasting, 7, 699-709, https://doi.org/10.1175/1520-0434(1992)007<0699:catcra>2.0.co;2, 1992.

Bessho, K., Date, K., Hayashi, M., Ikeda, A., Imai, T., Inoue, H., Kumagai, Y., Miyakawa, T., Murata, H., and Ohno, T.: An introduction to Himawari-8/9—Japan's new-generation geostationary meteorological satellites, Journal of the Meteorological Society of Japan. Ser. II, 94, 151-183, https://doi.org/10.2151/jmsj.2016-009, 2016.

Boutle, I., Price, J., Kudzotsa, I., Kokkola, H., and Romakkaniemi, S.: Aerosol–fog interaction and the transition to well-mixed radiation fog, Atmos. Chem. Phys., 18, 7827-7840, https://doi.org/10.5194/acp-18-7827-2018, 2018.

Boylan, J. W. and Russell, A. G.: PM and light extinction model performance metrics, goals, and criteria for three-dimensional air quality models, Atmos. Environ., 40, 4946-4959, https://doi.org/10.1016/j.atmosenv.2005.09.087, 2006.

Chaboureau, J.-P. and Bechtold, P.: A Simple Cloud Parameterization Derived from Cloud Resolving Model Data: Diagnostic and Prognostic Applications, J. Atmos. Sci., 59, 2362-2372, https://doi.org/10.1175/1520-0469(2002)059<2362:ascpdf>2.0.co;2, 2002.

Ding, Q., Sun, J., Huang, X., Ding, A., Zou, J., Yang, X., and Fu, C.: Impacts of black carbon on the formation of advection–radiation fog during a haze pollution episode in eastern China, Atmos. Chem. Phys., 19, 7759-7774, https://doi.org/10.5194/acp-19-7759-2019, 2019.

Ducongé, L., Lac, C., Vié, B., Bergot, T., and Price, J. D.: Fog in heterogeneous environments: the relative importance of local and non-local processes on radiative-advective fog formation, Q. J. R. Meteorolog. Soc., 146, 2522-2546, https://doi.org/10.1002/qj.3783, 2020.

Fernando, H. J. S., Gultepe, I., Dorman, C., Pardyjak, E., Wang, Q., Hoch, S. W., Richter, D., Creegan, E., Gaberšek, S., Bullock, T., Hocut, C., Chang, R., Alappattu, D., Dimitrova, R., Flagg, D., Grachev, A., Krishnamurthy, R., Singh, D. K., Lozovatsky, I., Nagare, B., Sharma, A., Wagh, S., Wainwright, C., Wroblewski, M., Yamaguchi, R., Bardoel, S., Coppersmith,

R. S., Chisholm, N., Gonzalez, E., Gunawardena, N., Hyde, O., Morrison, T., Olson, A., Perelet, A., Perrie, W., Wang, S., and Wauer, B.: C-FOG: Life of Coastal Fog, Bull. Am. Meteorol. Soc., 102, E244-E272, https://doi.org/10.1175/bams-d-19-0070.1, 2021.

Fitzjarrald, D. R. and Lala, G. G.: Hudson Valley Fog Environments, J. Appl. Meteorol. Clim., 28, 1303-1328, https://doi.org/10.1175/1520-0450(1989)028<1303:hvfe>2.0.co;2, 1989.

Gao, M., Carmichael, G. R., Wang, Y., Saide, P. E., Yu, M., Xin, J., Liu, Z., and Wang, Z.: Modeling study of the 2010 regional haze event in the North China Plain, Atmos. Chem. Phys., 16, 1673-1691, https://doi.org/10.5194/acp-16-1673-2016, 2016.

Garrett, T. J. and Zhao, C.: Increased Arctic cloud longwave emissivity associated with pollution from mid-latitudes, Nature, 440, 787-789, https://doi.org/10.1038/nature04636, 2006.

Ghan, S., Wang, M., Zhang, S., Ferrachat, S., Gettelman, A., Griesfeller, J., Kipling, Z., Lohmann, U., Morrison, H., and Neubauer, D.: Challenges in constraining anthropogenic aerosol effects on cloud radiative forcing using present-day spatiotemporal variability, Proc. Natl. Acad. Sci. U.S.A., 113, 5804-5811, https://doi.org/10.1073/pnas.1514036113, 2016.

Grell, G. A. and Dévényi, D.: A generalized approach to parameterizing convection combining ensemble and data assimilation techniques, Geophys. Res. Lett., 29, 38-31-38-34, https://doi.org/10.1029/2002gl015311, 2002.

Gultepe, I., Kuhn, T., Pavolonis, M., Calvert, C., Gurka, J., Heymsfield, A. J., Liu, P. S. K., Zhou, B., Ware, R., Ferrier, B., Milbrandt, J., and Bernstein, B.: Ice Fog in Arctic During FRAM–Ice Fog Project: Aviation and Nowcasting Applications, Bull. Am. Meteorol. Soc., 95, 211-226, https://doi.org/10.1175/bams-d-11-00071.1, 2014.

Guo, L., Guo, X., Fang, C., and Zhu, S.: Observation analysis on characteristics of formation, evolution and transition of a long-lasting severe fog and haze episode in North China, Sci. China, Ser. D Earth Sci., 58, 329-344, https://doi.org/10.1007/s11430-014-4924-2, 2015.

557 Guo, L., Guo, X., Luan, T., Zhu, S., and Lyu, K.: Radiative effects of clouds and fog on long-
558   lasting heavy fog events in northern China, Atmos. Res., 252, 105444,
559   https://doi.org/10.1016/j.atmosres.2020.105444, 2021.

560 Haeffelin, M., Bergot, T., Elias, T., Tardif, R., Carrer, D., Chazette, P., Colomb, M., Drobinski,
561   P., Dupont, E., Dupont, J.-C., Gomes, L., Musson-Genon, L., Pietras, C., Plana-Fattori, A.,
562   Protat, A., Rangognio, J., Raut, J.-C., Rémy, S., Richard, D., Sciare, J., and Zhang, X.:
563   Parisfog: Shedding new Light on Fog Physical Processes, Bull. Am. Meteorol. Soc., 91, 767-
564   783, https://doi.org/10.1175/2009bams2671.1, 2010.

565 Hammer, E., Gysel, M., Roberts, G. C., Elias, T., Hofer, J., Hoyle, C. R., Bukowiecki, N.,
566   Dupont, J. C., Burnet, F., Baltensperger, U., and Weingartner, E.: Size-dependent particle
567   activation properties in fog during the ParisFog 2012/13 field campaign, Atmos. Chem.
568   Phys., 14, 10517-10533, https://doi.org/10.5194/acp-14-10517-2014, 2014.

569 Holets, S. and Swanson, R. N.: High-Inversion Fog Episodes in Central California, J. Appl.
570   Meteorol.   Clim.,   20,   890-899,   https://doi.org/10.1175/1520-
571   0450(1981)020<0890:hifeic>2.0.co;2, 1981.

572 Hu, W., Zhao, T., Bai, Y., Kong, S., Xiong, J., Sun, X., Yang, Q., Gu, Y., and Lu, H.:
573   Importance of regional PM2.5 transport and precipitation washout in heavy air pollution in
574   the Twain-Hu Basin over Central China: Observational analysis and WRF-Chem simulation,
575   Sci. Total Environ., 758, 143710, https://doi.org/10.1016/j.scitotenv.2020.143710, 2021.

576 Iacono, M. J., Delamere, J. S., Mlawer, E. J., Shephard, M. W., Clough, S. A., and Collins, W.
577   D.: Radiative forcing by long-lived greenhouse gases: Calculations with the AER radiative
578   transfer models, J. Geophys. Res., 113, https://doi.org/10.1029/2008jd009944, 2008.

579 Iwabuchi, H., Putri, N. S., Saito, M., Tokoro, Y., Sekiguchi, M., Yang, P., and Baum, B. A.:
580   Cloud property retrieval from multiband infrared measurements by Himawari-8, Journal of
581   the Meteorological Society of Japan. Ser. II, https://doi.org/10.2151/jmsj.2018-001, 2018.

Jia, X., Quan, J., Zheng, Z., Liu, X., Liu, Q., He, H., and Liu, Y.: Impacts of Anthropogenic Aerosols on Fog in North China Plain, J. Geophys. Res.: Atmos., 124, 252-265, https://doi.org/10.1029/2018jd029437, 2019.

Kim, C. K. and Yum, S. S.: Local meteorological and synoptic characteristics of fogs formed over Incheon international airport in the west coast of Korea, Adv. Atmos. Sci., 27, 761-776, https://doi.org/10.1007/s00376-009-9090-7, 2010.

Kim, C. K. and Yum, S. S.: A numerical study of sea-fog formation over cold sea surface using a one-dimensional turbulence model coupled with the weather research and forecasting model, Boundary Layer Meteorol., 143, 481-505, https://doi.org/10.1007/s10546-012-9706-9, 2012.

Kim, C. K. and Yum, S. S.: A study on the transition mechanism of a stratus cloud into a warm sea fog using a single column model PAFOG coupled with WRF, Asia-Pac. J. Atmos. Sci., 49, 245-257, https://doi.org/10.1007/s13143-013-0024-z, 2013.

Kumar, B., Bera, S., Prabha, T. V., and Grabowski, W. W.: Cloud-edge mixing: Direct numerical simulation and observations in Indian Monsoon clouds, J. Adv. Model. Earth Syst., 9, 332-353, https://doi.org/10.1002/2016ms000731, 2017.

Kumar, B., Ranjan, R., Yau, M.-K., Bera, S., and Rao, S. A.: Impact of high- and low-vorticity turbulence on cloud–environment mixing and cloud microphysics processes, Atmos. Chem. Phys., 21, 12317-12329, https://doi.org/10.5194/acp-21-12317-2021, 2021.

Lee, H.-H., Chen, S.-H., Kleeman, M. J., Zhang, H., DeNero, S. P., and Joe, D. K.: Implementation of warm-cloud processes in a source-oriented WRF/Chem model to study the effect of aerosol mixing state on fog formation in the Central Valley of California, Atmos. Chem. Phys., 16, 8353-8374, https://doi.org/10.5194/acp-16-8353-2016, 2016.

Letu, H., Yang, K., Nakajima, T. Y., Ishimoto, H., Nagao, T. M., Riedi, J., Baran, A. J., Ma, R., Wang, T., and Shang, H.: High-resolution retrieval of cloud microphysical properties and

surface solar radiation using Himawari-8/AHI next-generation geostationary satellite, Remote Sens. Environ., 239, 111583, https://doi.org/10.1016/j.rse.2019.111583, 2020.

Li, M., Liu, H., Geng, G., Hong, C., Liu, F., Song, Y., Tong, D., Zheng, B., Cui, H., Man, H., Zhang, Q., and He, K.: Anthropogenic emission inventories in China: a review, Natl. Sci. Rev., 4, 834-866, https://doi.org/10.1093/nsr/nwx150, 2017a.

Li, Z., Guo, J., Ding, A., Liao, H., Liu, J., Sun, Y., Wang, T., Xue, H., Zhang, H., and Zhu, B.: Aerosol and boundary-layer interactions and impact on air quality, Natl. Sci. Rev., 4, 810-833, https://doi.org/10.1093/nsr/nwx117, 2017b.

Liu, D. Y., Niu, S. J., Yang, J., Zhao, L. J., Lü, J. J., and Lu, C. S.: Summary of a 4-Year Fog Field Study in Northern Nanjing, Part 1: Fog Boundary Layer, Pure Appl. Geophys., 169, 809-819, https://doi.org/10.1007/s00024-011-0343-x, 2011.

Liu, Y., Hua, S., Jia, R., and Huang, J.: Effect of Aerosols on the Ice Cloud Properties Over the Tibetan Plateau, J. Geophys. Res.: Atmos., 124, 9594-9608, https://doi.org/10.1029/2019jd030463, 2019.

Liu, Y., Zhu, Q., Hua, S., Alam, K., Dai, T., and Cheng, Y.: Tibetan Plateau driven impact of Taklimakan dust on northern rainfall, Atmos. Environ., 234, 117583, https://doi.org/10.1016/j.atmosenv.2020.117583, 2020.

Maalick, Z., Kühn, T., Korhonen, H., Kokkola, H., Laaksonen, A., and Romakkaniemi, S.: Effect of aerosol concentration and absorbing aerosol on the radiation fog life cycle, Atmos. Environ., 133, 26-33, https://doi.org/10.1016/j.atmosenv.2016.03.018, 2016.

Maronga, B. and Bosveld, F. C.: Key parameters for the life cycle of nocturnal radiation fog: a comprehensive large-eddy simulation study, Q. J. R. Meteorolog. Soc., 143, 2463-2480, https://doi.org/10.1002/qj.3100, 2017.

Matsui, T., Zhang, S. Q., Lang, S. E., Tao, W.-K., Ichoku, C., and Peters-Lidard, C. D.: Impact of radiation frequency, precipitation radiative forcing, and radiation column aggregation on

convection-permitting West African monsoon simulations, Clim. Dyn., 55, 193-213, https://doi.org/10.1007/s00382-018-4187-2, 2020.

Mazoyer, M., Burnet, F., and Denjean, C.: Experimental study on the evolution of droplet size distribution during the fog life cycle, Atmos. Chem. Phys., 22, 11305-11321, https://doi.org/10.5194/acp-22-11305-2022, 2022.

Mazoyer, M., Lac, C., Thouron, O., Bergot, T., Masson, V., and Musson-Genon, L.: Large eddy simulation of radiation fog: impact of dynamics on the fog life cycle, Atmos. Chem. Phys., 17, 13017-13035, https://doi.org/10.5194/acp-17-13017-2017, 2017.

Mazoyer, M., Burnet, F., Denjean, C., Roberts, G. C., Haeffelin, M., Dupont, J.-C., and Elias, T.: Experimental study of the aerosol impact on fog microphysics, Atmos. Chem. Phys., 19, 4323-4344, https://doi.org/10.5194/acp-19-4323-2019, 2019.

Mecikalski, J. R., Bedka, K. M., Paech, S. J., and Litten, L. A.: A Statistical Evaluation of GOES Cloud-Top Properties for Nowcasting Convective Initiation, Mon. Weather Rev., 136, 4899-4914, https://doi.org/10.1175/2008mwr2352.1, 2008.

Morrison, H., Curry, J., and Khvorostyanov, V.: A new double-moment microphysics parameterization for application in cloud and climate models. Part I: Description, J. Atmos. Sci., 62, 1665-1677, https://doi.org/10.1175/JAS3446.1, 2005.

Nakanishi, M. and Niino, H.: Development of an Improved Turbulence Closure Model for the Atmospheric Boundary Layer, J. Meteorolog. Soc. Jpn., 87, 895-912, https://doi.org/10.2151/jmsj.87.895, 2009.

Niu, S., Lu, C., Yu, H., Zhao, L., and Lü, J.: Fog research in China: An overview, Adv. Atmos. Sci., 27, 639-662, https://doi.org/10.1007/s00376-009-8174-8, 2010.

Niu, S. J., Liu, D. Y., Zhao, L. J., Lu, C. S., Lü, J. J., and Yang, J.: Summary of a 4-Year Fog Field Study in Northern Nanjing, Part 2: Fog Microphysics, Pure Appl. Geophys., 169, 1137-1155, https://doi.org/10.1007/s00024-011-0344-9, 2011.

Petters, J. L., Harrington, J. Y., and Clothiaux, E. E.: Radiative–dynamical feedbacks in low liquid water path stratiform clouds, J. Atmos. Sci., 69, 1498-1512, https://doi.org/10.1175/JAS-D-11-0169.1, 2012.

Petters, M. D. and Kreidenweis, S. M.: A single parameter representation of hygroscopic growth and cloud condensation nucleus activity, Atmos. Chem. Phys., 7, 1961-1971, https://doi.org/10.5194/acp-7-1961-2007, 2007.

Porson, A., Price, J., Lock, A., and Clark, P.: Radiation Fog. Part II: Large-Eddy Simulations in Very Stable Conditions, Boundary Layer Meteorol., 139, 193-224, https://doi.org/10.1007/s10546-010-9579-8, 2011.

Prabhakaran, P., Hoffmann, F., and Feingold, G.: Evaluation of Pulse Aerosol Forcing on Marine Stratocumulus Clouds in the Context of Marine Cloud Brightening, J. Atmos. Sci., 80, 1585-1604, https://doi.org/10.1175/JAS-D-22-0207.1, 2023.

Price, J. D., Lane, S., Boutle, I. A., Smith, D. K. E., Bergot, T., Lac, C., Duconge, L., McGregor, J., Kerr-Munslow, A., Pickering, M., and Clark, R.: LANFEX: A Field and Modeling Study to Improve Our Understanding and Forecasting of Radiation Fog, Bull. Am. Meteorol. Soc., 99, 2061-2077, https://doi.org/10.1175/bams-d-16-0299.1, 2018.

Quan, J., Zhang, Q., He, H., Liu, J., Huang, M., and Jin, H.: Analysis of the formation of fog and haze in North China Plain (NCP), Atmos. Chem. Phys., 11, 8205-8214, https://doi.org/10.5194/acp-11-8205-2011, 2011.

Quan, J., Liu, Y., Jia, X., Liu, L., Dou, Y., Xin, J., and Seinfeld, J. H.: Anthropogenic aerosols prolong fog lifetime in China, Environ. Res. Lett., 16, 044048, https://doi.org/10.1088/1748-9326/abef32, 2021.

Roach, W., Brown, R., Caughey, S., Garland, J., and Readings, C.: The physics of radiation fog: I–a field study, Q. J. R. Meteorolog. Soc., 102, 313-333, https://doi.org/10.1002/qj.49710243204, 1976.

Shen, C., Zhao, C., Ma, N., Tao, J., Zhao, G., Yu, Y., and Kuang, Y.: Method to Estimate Water Vapor Supersaturation in the Ambient Activation Process Using Aerosol and Droplet Measurement Data, J. Geophys. Res.: Atmos., 123, https://doi.org/10.1029/2018jd028315, 2018.

Simmel, M. and Wurzler, S.: Condensation and activation in sectional cloud microphysical models, Atmos. Res., 80, 218-236, https://doi.org/10.1016/j.atmosres.2005.08.002, 2006.

Steeneveld, G. J. and de Bode, M.: Unravelling the relative roles of physical processes in modelling the life cycle of a warm radiation fog, Q. J. R. Meteorolog. Soc., 144, 1539-1554, https://doi.org/10.1002/qj.3300, 2018.

Stolaki, S., Haeffelin, M., Lac, C., Dupont, J. C., Elias, T., and Masson, V.: Influence of aerosols on the life cycle of a radiation fog event. A numerical and observational study, Atmos. Res., 151, 146-161, https://doi.org/10.1016/j.atmosres.2014.04.013, 2015.

Toll, V., Christensen, M., Quaas, J., and Bellouin, N.: Weak average liquid-cloud-water response to anthropogenic aerosols, Nature, 572, 51-55, https://doi.org/10.1038/s41586-019-1423-9, 2019.

Twomey, S.: The influence of pollution on the shortwave albedo of clouds, J. Atmos. Sci., 34, 1149-1152, https://doi.org/10.1175/1520-0469(1977)034<1149:TIOPOT>2.0.CO;2, 1977.

Vautard, R., Yiou, P., and van Oldenborgh, G. J.: Decline of fog, mist and haze in Europe over the past 30 years, Nat. Geosci., 2, 115-119, https://doi.org/10.1038/ngeo414, 2009.

Wærsted, E. G., Haeffelin, M., Dupont, J.-C., Delanoë, J., and Dubuisson, P.: Radiation in fog: quantification of the impact on fog liquid water based on ground-based remote sensing, Atmos. Chem. Phys., 17, 10811-10835, https://doi.org/10.5194/acp-17-10811-2017, 2017.

Wang, Y., Fan, J., Zhang, R., Leung, L. R., and Franklin, C.: Improving bulk microphysics parameterizations in simulations of aerosol effects, J. Geophys. Res.: Atmos., 118, 5361-5379, https://doi.org/10.1002/jgrd.50432, 2013.

707 Wang, Y., Lu, C., Niu, S., Lv, J., Jia, X., Xu, X., Xue, Y., Zhu, L., and Yan, S.: Diverse
708   dispersion effects and parameterization of relative dispersion in urban fog in eastern China,
709   J. Geophys. Res.: Atmos., n/a, e2022JD037514, https://doi.org/10.1029/2022JD037514,
710   2023.
711 Wang, Y., Vogel, J. M., Lin, Y., Pan, B., Hu, J., Liu, Y., Dong, X., Jiang, J. H., Yung, Y. L.,
712   and Zhang, R.: Aerosol microphysical and radiative effects on continental cloud ensembles,
713   Adv. Atmos. Sci., 35, 234-247, https://doi.org/10.1007/s00376-017-7091-5, 2018.
714 Wang, Y., Niu, S., Lu, C., Lv, J., Zhang, J., Zhang, H., Zhang, S., Shao, N., Sun, W., Jin, Y.,
715   and Song, Q.: Observational study of the physical and chemical characteristics of the winter
716   radiation fog in the tropical rainforest in Xishuangbanna, China, Sci. China, Ser. D Earth
717   Sci., 64, 1982-1995, https://doi.org/10.1007/s11430-020-9766-4, 2021.
718 WMO: International meteorological vocabulary, WMO-182, 784 pp., 1992.
719 Xu, X., Lu, C., Liu, Y., Gao, W., Wang, Y., Cheng, Y., Luo, S., and Van Weverberg, K.: Effects
720   of Cloud Liquid-Phase Microphysical Processes in Mixed-Phase Cumuli Over the Tibetan
721   Plateau, J. Geophys. Res.: Atmos., 125, https://doi.org/10.1029/2020jd033371, 2020.
722 Yamane, Y., Hayashi, T., Dewan, A. M., and Akter, F.: Severe local convective storms in
723   Bangladesh: Part II, Atmos. Res., 95, 407-418,
724   https://doi.org/10.1016/j.atmosres.2009.11.003, 2010.
725 Yan, S., Zhu, B., Huang, Y., Zhu, J., Kang, H., Lu, C., and Zhu, T.: To what extents do
726   urbanization and air pollution affect fog?, Atmos. Chem. Phys., 20, 5559-5572,
727   https://doi.org/10.5194/acp-20-5559-2020, 2020.
728 Yan, S., Zhu, B., Zhu, T., Shi, C., Liu, D., Kang, H., Lu, W., and Lu, C.: The Effect of Aerosols
729   on Fog Lifetime: Observational Evidence and Model Simulations, Geophys. Res. Lett., 48,
730   https://doi.org/10.1029/2020gl091156, 2021.
731 Yang, Q., Zhao, T., Tian, Z., Kumar, K. R., Chang, J., Hu, W., Shu, Z., and Hu, J.: The Cross-
732   Border Transport of PM2.5 from the Southeast Asian Biomass Burning Emissions and Its

733   Impact on Air Pollution in Yunnan Plateau, Southwest China, Remote Sens., 14, 1886,

734   https://doi.org/10.3390/rs14081886, 2022.

735 Yang, Y., Zhao, C., and Fan, H.: Spatiotemporal distributions of cloud properties over China

736   based on Himawari-8 advanced Himawari imager data, Atmos. Res., 240, 104927,

737   https://doi.org/10.1016/j.atmosres.2020.104927, 2020.

738 Yang, Y., Hu, X.-M., Gao, S., and Wang, Y.: Sensitivity of WRF simulations with the YSU

739   PBL scheme to the lowest model level height for a sea fog event over the Yellow Sea, Atmos.

740   Res., 215, 253-267, https://doi.org/10.1016/j.atmosres.2018.09.004, 2019.

741 Ye, X., Wu, B., and Zhang, H.: The turbulent structure and transport in fog layers observed

742   over   the   Tianjin   area,   Atmos.   Res.,   153,   217-234,

743   https://doi.org/10.1016/j.atmosres.2014.08.003, 2015.

744 Yum, S. S. and Hudson, J. G.: Adiabatic predictions and observations of cloud droplet spectral

745   broadness, Atmos. Res., 73, 203-223, https://doi.org/10.1016/j.atmosres.2004.10.006, 2005.

746 Zaveri, R. A. and Peters, L. K.: A new lumped structure photochemical mechanism for large-

747   scale   applications,   J.   Geophys.   Res.:   Atmos.,   104,   30387-30415,

748   https://doi.org/10.1029/1999jd900876, 1999.

749 Zaveri, R. A., Easter, R. C., Fast, J. D., and Peters, L. K.: Model for Simulating Aerosol

750   Interactions   and   Chemistry   (MOSAIC),   J.   Geophys.   Res.,   113,

751   https://doi.org/10.1029/2007jd008782, 2008.

752 Zhao, C. and Garrett, T. J.: Effects of Arctic haze on surface cloud radiative forcing, Geophys.

753   Res. Lett., 42, 557-564, https://doi.org/10.1002/2014gl062015, 2015.

754 Zhao, L., Niu, S., Zhang, Y., and Xu, F.: Microphysical characteristics of sea fog over the east

755   coast   of   Leizhou   Peninsula,   China,   Adv.   Atmos.   Sci.,   30,   1154-1172,

756   https://doi.org/10.1007/s00376-012-1266-x, 2013.

757 Zhao, L., Zhao, C., Wang, Y., Wang, Y., and Yang, Y.: Evaluation of cloud microphysical

758   properties derived from MODIS and Himawari-8 using in situ aircraft measurements over

the Southern Ocean, Earth Space Sci., 7, e2020EA001137, https://doi.org/10.1029/2020EA001137, 2020.

Zheng, B., Tong, D., Li, M., Liu, F., Hong, C., Geng, G., Li, H., Li, X., Peng, L., Qi, J., Yan, L., Zhang, Y., Zhao, H., Zheng, Y., He, K., and Zhang, Q.: Trends in China's anthropogenic emissions since 2010 as the consequence of clean air actions, Atmos. Chem. Phys., 18, 14095-14111, https://doi.org/10.5194/acp-18-14095-2018, 2018.

Zhong, J., Zhang, X., Wang, Y., Liu, C., and Dong, Y.: Heavy aerosol pollution episodes in winter Beijing enhanced by radiative cooling effects of aerosols, Atmos. Res., 209, 59-64, https://doi.org/10.1016/j.atmosres.2018.03.011, 2018.

Zhou, B. and Ferrier, B. S.: Asymptotic Analysis of Equilibrium in Radiation Fog, J. Appl. Meteorol. Clim., 47, 1704-1722, https://doi.org/10.1175/2007jamc1685.1, 2008.

Zhu, J., Zhu, B., Huang, Y., An, J., and Xu, J.: PM2.5 vertical variation during a fog episode in a rural area of the Yangtze River Delta, China, Sci. Total Environ., 685, 555-563, https://doi.org/10.1016/j.scitotenv.2019.05.319, 2019.

787 **Table 1.** Summary of major parameterisation schemes.

Scheme	Option
Microphysics	Morrison
Boundary layer	MYNN
Short-wave radiation	Goddard
Long-wave radiation	RRTMG
Cumulus	Grell 3D
Aerosol chemistry	MOSAIC (4 bins)
Gas phase chemistry	CBMZ

788

789

790

791

792

793

794

795

796

797

798

799 **Table 2.** Evaluation of PM$_{2.5}$ mass concentration. NMB, NME, MFB, and MFE stand for
800 normalised mean bias, normalised mean error, mean fractional bias, and mean fractional error,
801 respectively. Time '2514' (DateHour) indicates 14:00 local standard time (LST) (LST =
802 Universal Time Coordinated + 8 h) on 25 November 2018. The other time expressions follow
803 the same logic.

DateHour	NMB (%)	NME (%)	MFB (%)	MFE (%)
2514-2614	13	25	13	24
2614-2714	38	42	35	38
Total	25	30	24	28

804

805

806

807

808

809

810

811

812

813

814

815

816

Table 3. Elements a–d in the Heidke skill score calculation

	Fog observed	No fog observed
Fog simulated	a	b
No fog simulated	c	d

817

818

819

820

821

822

823

824

825

826

827

828

829

830

831

Table 4. Quantitative estimation of ACI strength in two fog events (Fog1 and Fog2), including the responses of fog optical depth (τ_c), liquid water path (LWP), and fog effective radius (R_e) to the changes in fog droplet number concentration (N_d). In EXP1, both fog events occur under polluted conditions, and fog events in EXP2 occur under clean conditions. In EXP3, Fog1 occurs under clean conditions and Fog2 occurs under polluted conditions. The ratio represents the relative change between Fog1 and Fog2, calculated as (Fog2 − Fog1)/Fog1. In the fourth and sixth columns, Fog1 in both EXP2 and EXP3 occur under clean conditions.

	EXP1 vs EXP2			EXP3 vs EXP2		
	Fog1	Fog2	Ratio	Fog1	Fog2	Ratio
$\Delta\ln\tau_c/\Delta\ln N_d$	0.98	1.32	34.7%	–	1.17	–
$\Delta\ln LWP/\Delta\ln N_d$	0.76	1.08	42.1%	–	1.00	–
$-\Delta\ln R_e/\Delta\ln N_d$	0.22	0.24	9.1%	–	0.17	–

845 **Table 5.** Average 2 m relative humidity (RH_{2m}) and planetary boundary layer height (PBLH)
846 above the ground in domain 03 during 12:00–20:00 local standard time (LST) (LST = Universal
847 Time Coordinated + 8 h) on 25 and 26 November 2018 under clean and polluted conditions.
848 DIF is the difference in each property between 25 and 26 November.

	Clean			Polluted		
	25 Nov	26 Nov	DIF	25 Nov	26 Nov	DIF
RH_{2m} (%)	76	80	4	76	82	6
PBLH (m)	669	610	−59	670	578	−92

849

850
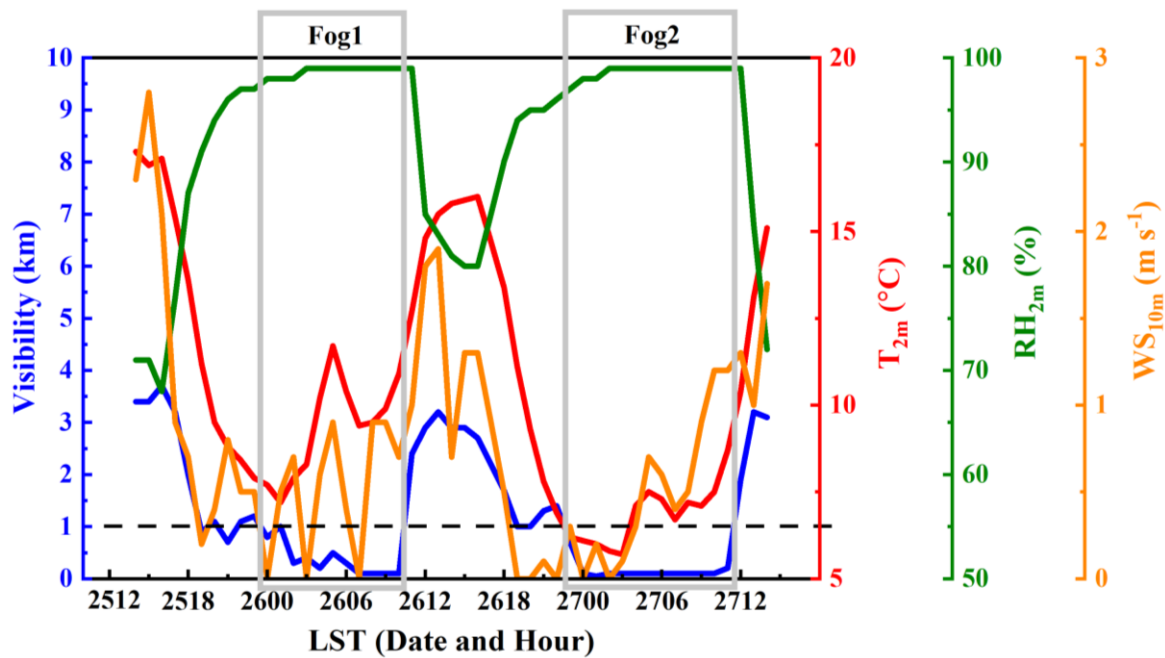
851

852 **Figure 1.** The timeseries of visibility, 2 m temperature (T_{2m}), 2 m relative humidity (RH_{2m}),

853 and 10 m wind speed (WS_{10m}) above the ground at the Nanjing observation site (31.93°N,

854 118.9°E). Fog1 and Fog2 in the light grey box are the two fog events. Time '2512' indicates

855 12:00 local standard time (LST) (LST = Universal Time Coordinated + 8 h) on 25 November

856 2018. The other time expressions follow the same logic.

857
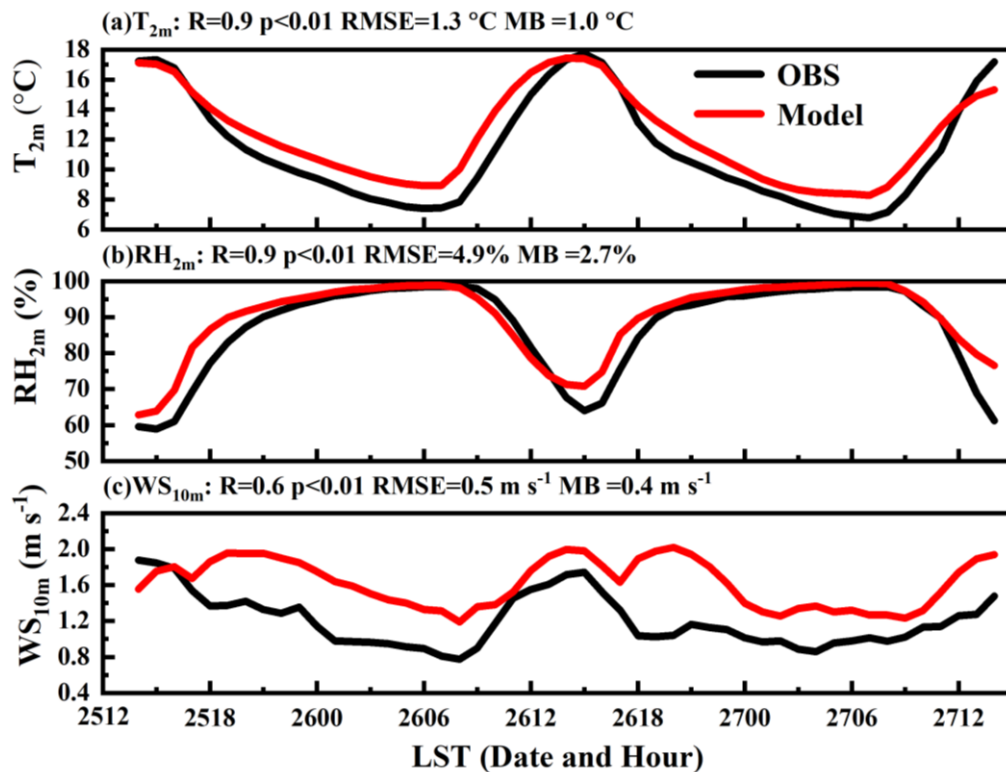
858

859   **Figure 2.** Hourly variations in observed (black lines) and simulated (red lines) meteorological

860   properties, including (a) 2 m temperature (T_{2m}), (b) 2 m relative humidity (RH_{2m}), and (c) 10 m

861   wind speed (WS_{10m}) above the ground, averaged over 104 meteorological stations in domain

862   03 from 14:00 local standard time (LST) (LST = Universal Time Coordinated + 8 h) on 25

863   November to 14:00 LST on 27 November 2018. R, p, RMSE, and MB indicate the correlation

864   coefficient, significance level, root-mean-square error, and mean bias, respectively. The

865   equations for RMSE and MB (Eq. S1-S2) are given in the supplement. Time '2512' indicates

866   12:00 LST on 25 November 2018. The other time expressions follow the same logic.

867
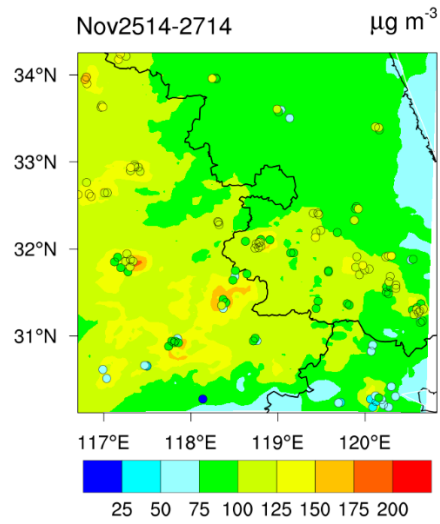
868

869 **Figure 3.** Simulated (shaded area) and observed (coloured dots) average distributions of PM$_{2.5}$

870 concentration (μg m^{-3}) from 14:00 local standard time (LST) (LST = Universal Time

871 Coordinated + 8 h) on 25 November to 14:00 LST on 27 November 2018.

872

873
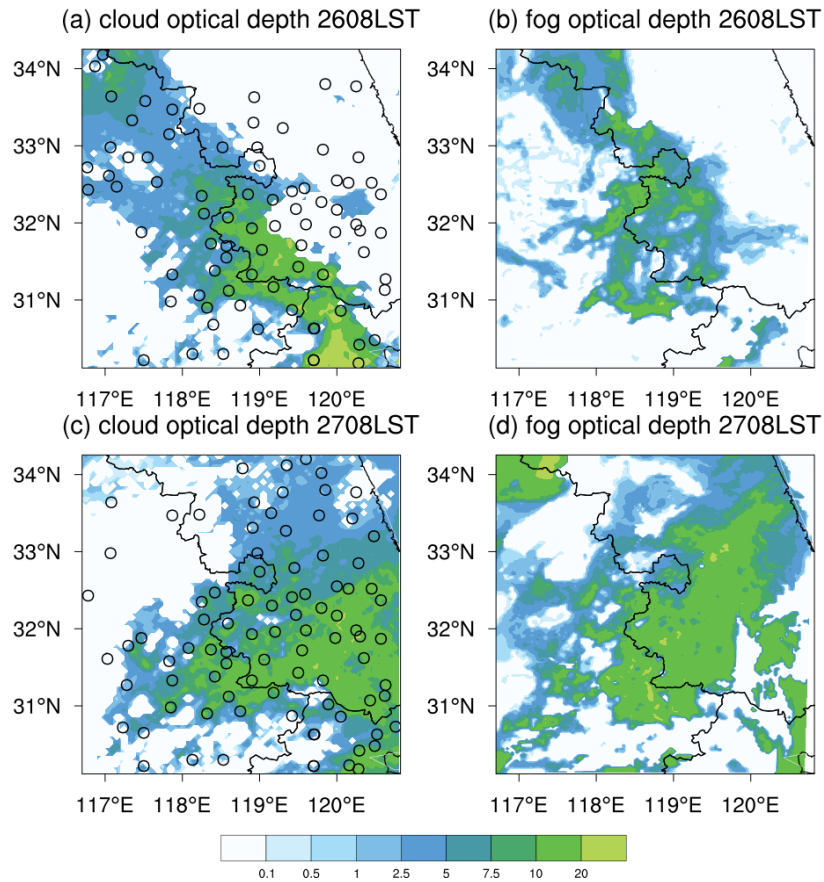
Figure 4. (a, c) Distributions of ground-based fog observations (the black circular points) and cloud optical depth from Himawari-8 products at 08:00 LST on 26 and 27 November 2018. (b, d) Simulated fog optical depth distributions in domain 03 at the corresponding time of observations. Time '2608LST' indicates 08:00 local standard time (LST) (LST = Universal Time Coordinated + 8 h) on 26 November 2018. The other time expressions follow the same logic.
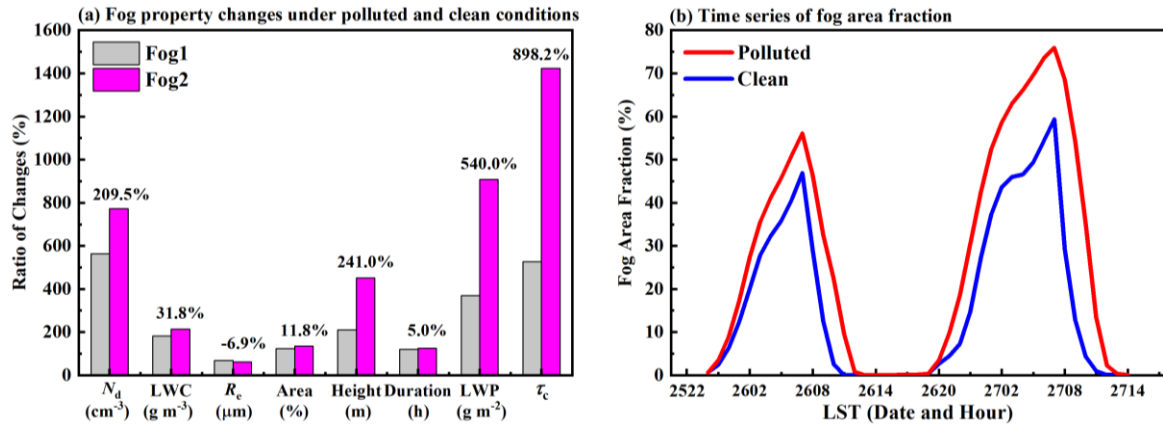
883
884 **Figure 5.** (a) Aerosol-induced changes in macro- and microphysical properties during the first

885 fog (Fog1) and the second fog (Fog2) events under polluted and clean conditions. (b) Temporal

886 evolution of fog area fraction under clean and polluted conditions. N_d, LWC, R_e, Area, Height,

887 Duration, LWP, and τ_c indicate fog droplet number concentration, liquid water content,

888 effective radius, fog area fraction, fog-top height, liquid water path, and fog optical depth,

889 respectively. The ratios of changes are calculated by Polluted/Clean in Fig. 5a which reveal the

890 aerosol-induced changes. The numbers above the bars in Fig. 5a represent the difference in

891 those ratios of changes between Fog1 and Fog2 (calculated by Fog2–Fog1). Time '2522' in Fig.

892 5b indicates 22:00 local standard time (LST) (LST = Universal Time Coordinated + 8 h) on 25

893 November 2018. The other time expressions follow the same logic.

894

895
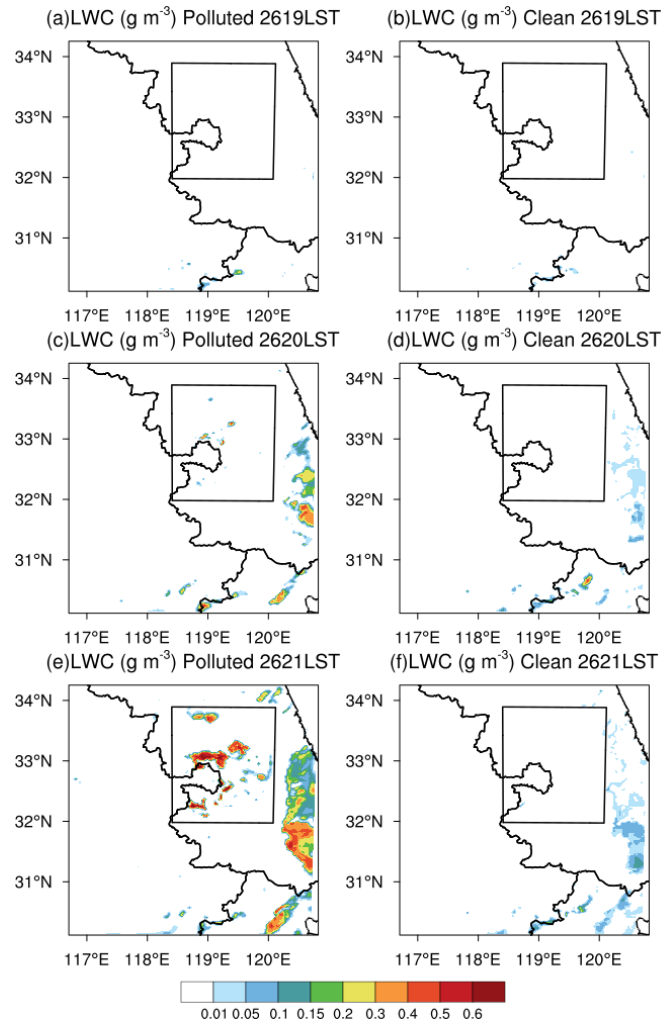
Figure 6. Liquid water content (LWC) distribution at the bottom layer from 19:00-21:00 local

standard time (LST) (LST = Universal Time Coordinated + 8 h) on 26 November 2018 under

(a, c, e) polluted and (b, d, f) clean conditions. The black box is the area in which Fog2 formed

earlier under polluted conditions. Time '2619LST' indicates 19:00 LST on 26 November 2018.

The other time expressions follow the same logic.

901

902
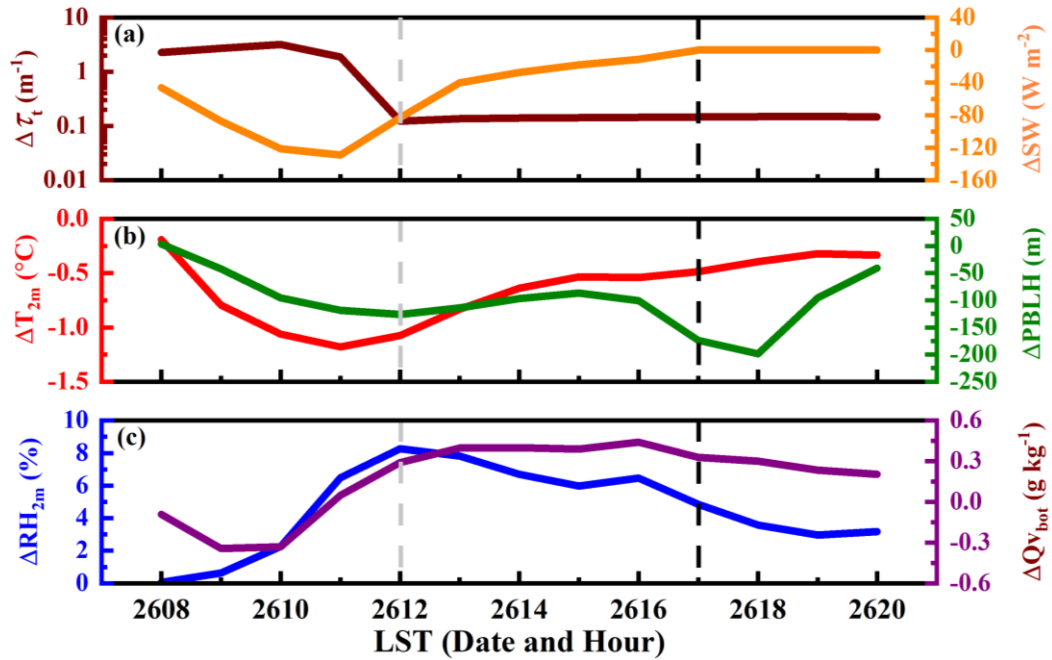
Figure 7. Differences in properties between polluted and clean conditions in the black box in Fig. 6, including (a) total optical depth (τ_t), surface downwelling short-wave radiation (SW), (b) 2 m temperature (T_{2m}), planetary boundary layer height (PBLH), (c) 2 m relative humidity (RH_{2m}), and water vapour mixing ratio at the bottom of the model (Qv_{bot}), where $\tau_t = \tau_c$ (fog optical depth) + AOD (aerosol optical depth). The grey dashed line is the time of complete evaporation of Fog1 under polluted conditions. The black dashed line is the time of sunset. Time '2608' indicates 08:00 local standard time (LST) (LST = Universal Time Coordinated + 8 h) on 26 November 2018. The other time expressions follow the same logic.

911

912
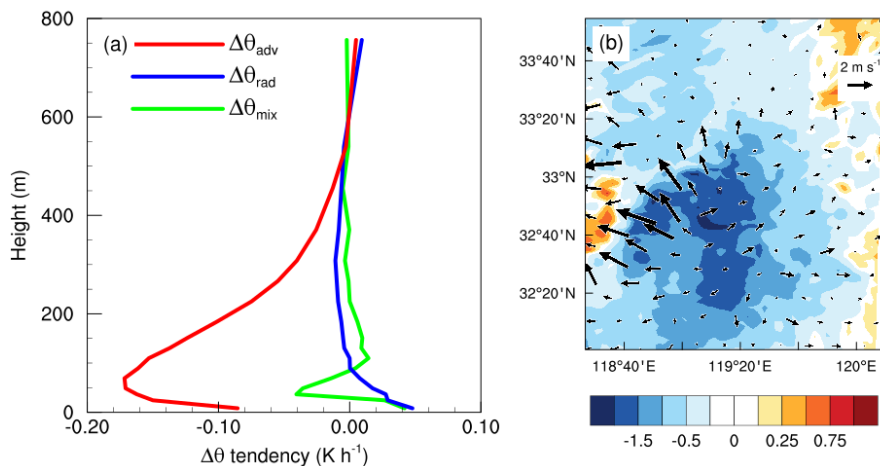
Figure 8. (a) Differences (Polluted − Clean) in terms contributing to the potential temperature tendency, including radiation (θ_{rad}), vertical mixing (θ_{mix}), and advection (θ_{adv}) in the black box in Fig. 6 before fog formation (17:00–19:00 local standard time [LST = Universal Time Coordinated + 8 h]). (b) The shaded area represents the mean temperature difference (Polluted − Clean), and vectors represent the mean wind vector difference (Polluted − Clean) at the bottom of the model.

913
914
915
916
917
918
919
920
921

922
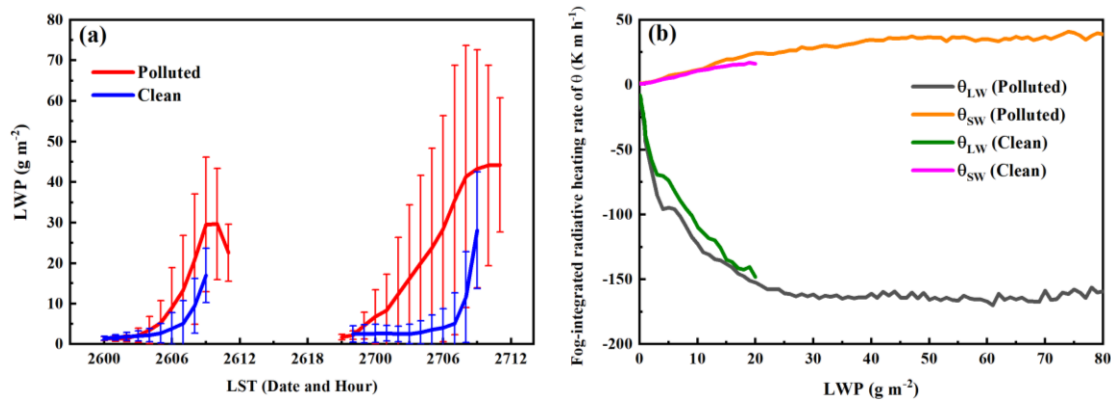
Figure 9. (a) The timeseries of liquid water path (LWP) under polluted and clean conditions. The length of the bar represents standard deviation. (b) Dependence of fog-integrated radiative cooling or heating with LWP under polluted and clean conditions. θ_{LW} and θ_{SW} represent vertically integrated heating rate of potential temperature (θ) within the fog layer due to long-wave radiation and short-wave radiation, respectively. Time '2512' indicates 12:00 local standard time (LST) (LST = Universal Time Coordinated + 8 h) on 25 November 2018. The other time expressions follow the same logic.

930

931
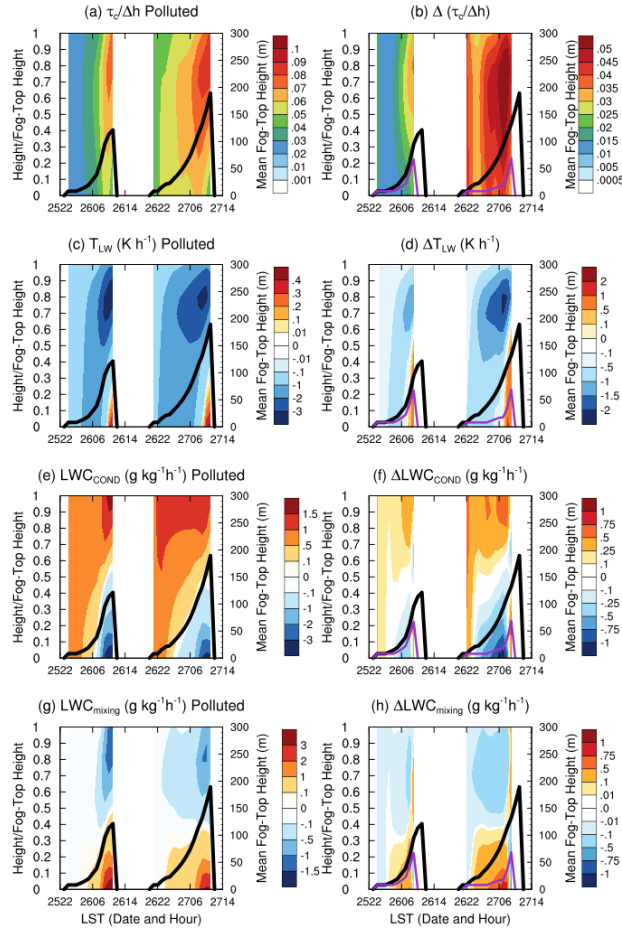
Figure 10. Time-height profiles of (a-b) average extinction coefficient through the fog layers, which is fog optical depth (τ_c) at per unit height ($\tau_c/\Delta h$), (c-d) radiative cooling rate (T_{LW}), (e-f) condensation growth rate (LWC_{COND}), and (g-h) liquid water content tendency due to vertical mixing (LWC_{mixing}). Heights on the left axes are normalised by the fog-top heights and the left axes are mean fog-top heights. The left column represents polluted conditions and the right column represents the difference (Polluted − Clean). Black and purple lines are the mean fog top heights under polluted and clean conditions, respectively. Time '2522' indicates 22:00 local standard time (LST) (LST = Universal Time Coordinated + 8 h) on 25 November 2018. The other time expressions follow the same logic.
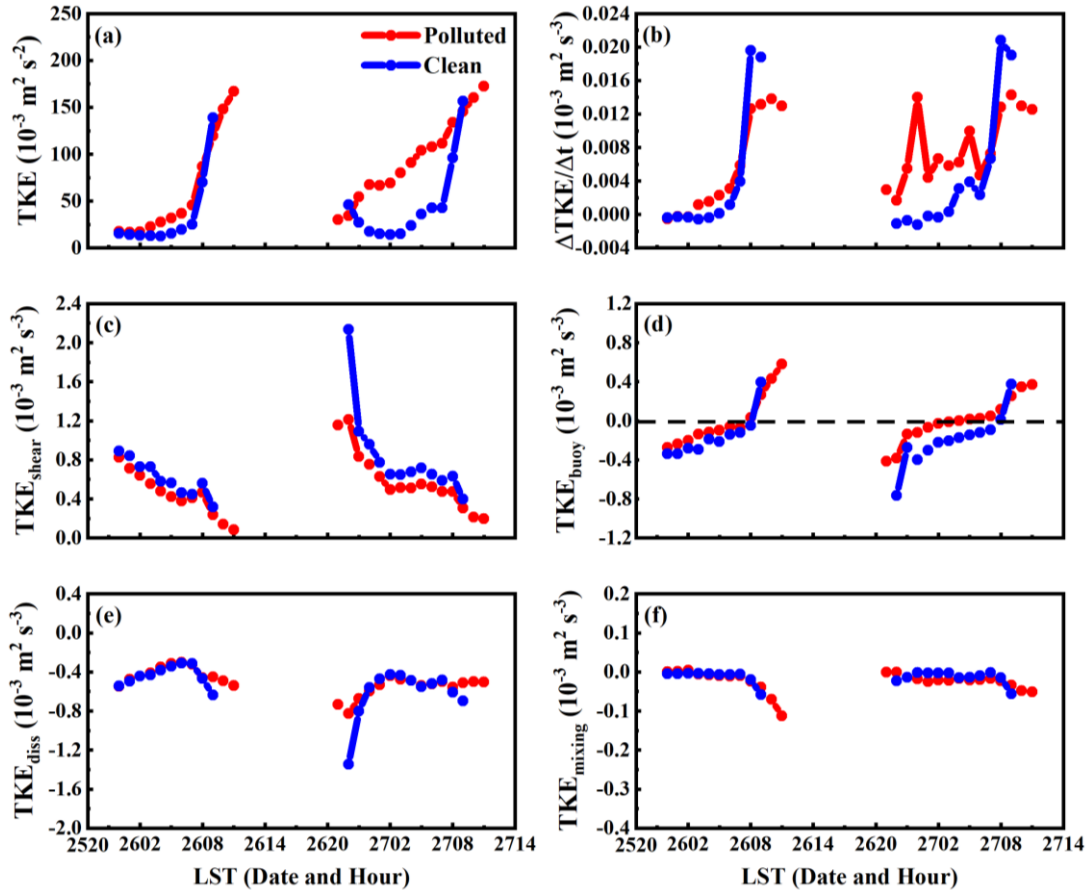
Figure 11. (a) Temporal evolution of turbulent kinetic energy (TKE), (b) TKE tendency, (c) wind shear term (TKE$_{shear}$), (d) buoyancy term (TKE$_{buoy}$), (e) dissipation term (TKE$_{diss}$), and (f) vertical mixing terms (TKE$_{mixing}$) under polluted and clean conditions. The dashed line represents the zero line for TKE$_{buoy}$. Time '2522' indicates 22:00 local standard time (LST) (LST = Universal Time Coordinated + 8 h) on 25 November 2018. The other time expressions follow the same logic.
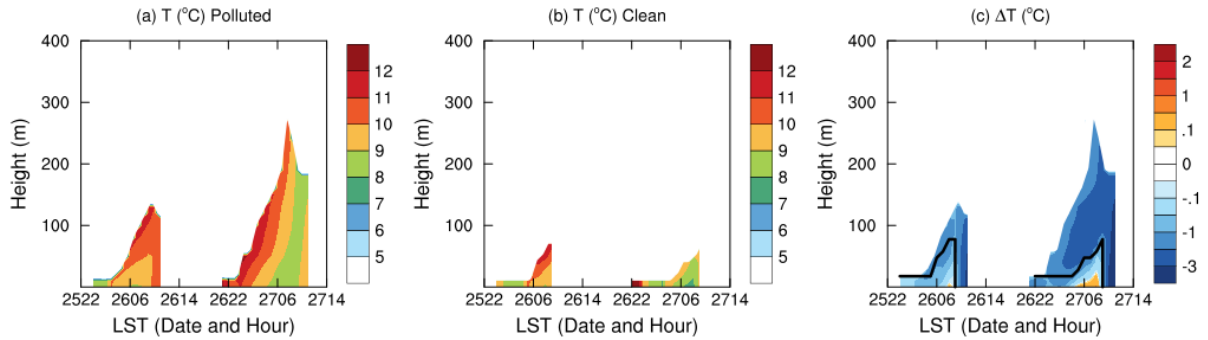
950

951 **Figure 12.** Time-height profiles of in-fog temperature (T) under (a) polluted and (b) clean
952 conditions. (c) Difference between polluted and clean conditions. The Black line on the right
953 side represents the maximal fog-top height under clean conditions. Time '2522' indicates 22:00
954 local standard time (LST) (LST = Universal Time Coordinated + 8 h) on 25 November 2018.
955 The other time expressions follow the same logic.

956

957
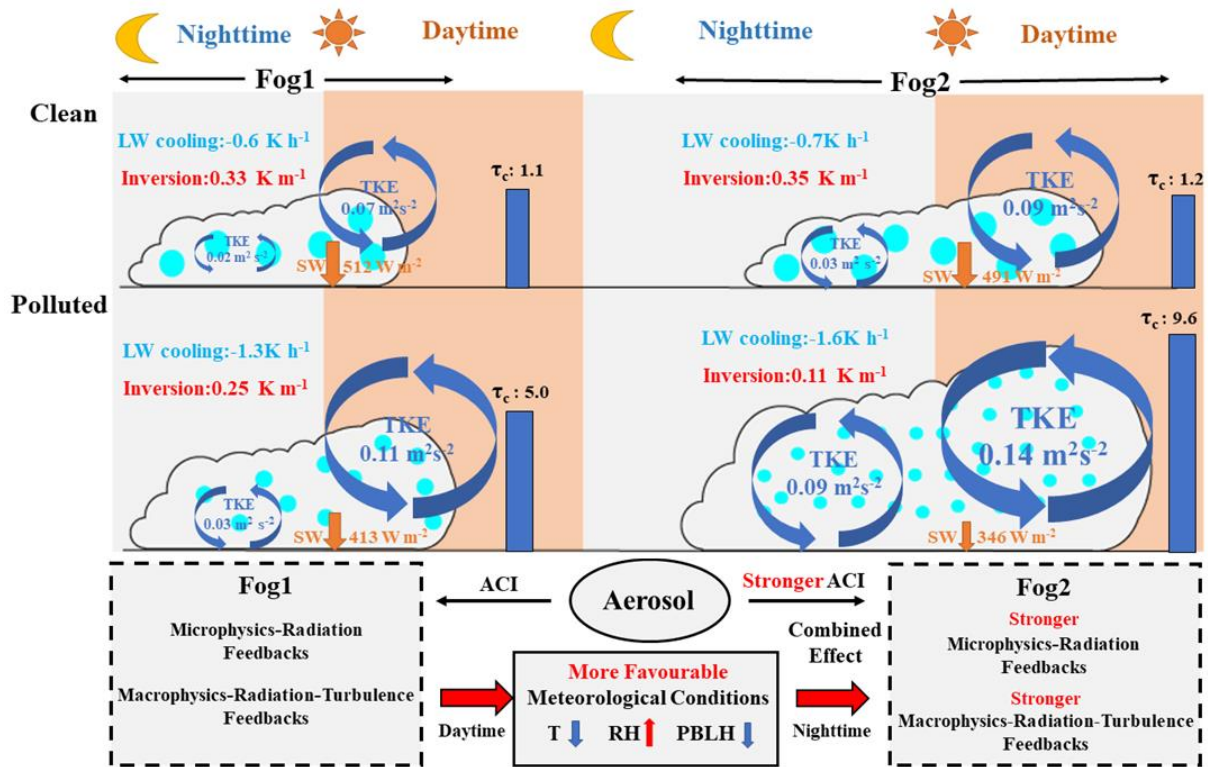
Figure 13. Conceptual image of interactions between aerosol–fog interaction (ACI) and planetary boundary layer (PBL). τ_c, SW, LW, TKE, T, RH, and PBLH stand for fog optical depth, short-wave radiation, long-wave radiation, turbulent kinetic energy, temperature, relative humidity, and planetary boundary layer height, respectively. LW and inversion are calculated at night time, and τ_c is calculated at daytime.

963

964